

A close-packed sphere model for characterising porous networks in atomistic simulations and its application in energy storage and conversion

Manikantan R. Nair^{a,†}, Ayush Khaitan^{a,†}, Ayush Owhal^{a,b}, Inturi Ramesh Chandra^a, Sachin U. Belgamwar^a, Radha Raman Mishra^a, Saurav Goel^{c,d+} and Tribeni Roy^{a,c,e*}

^aDepartment of Mechanical Engineering, Birla Institute of Technology and Science Pilani, Rajasthan 333031, India

^bDepartment of Mechanical Engineering, SD Bansal College, Indore, 452001, India

^cLondon South Bank University, 103 Borough Road, London SE1 0AA, UK

^dUniversity of Petroleum and Energy Studies, Dehradun 248007, India

^eSchool of Interdisciplinary Research and Entrepreneurship (SIRE), BITS Pilani, Rajasthan 333031, India

[†]Equal contributions: Authors contributed equally to this work.

Corresponding author: *GOELS@Lsbu.ac.uk and *tribeni.roy@pilani.bits-pilani.ac.in

Abstract

Hierarchical (micro, meso & macro) porosity in materials plays a crucial role in influencing the movement of ions which governs the energy and power density during energy storage and conversion. The extant available methods to characterise porosity across scales (nano to meso to macro) lacks rigour and accuracy. Having accurate assessment of the porosity in materials can unlock new designs of electrodes for energy efficient energy storage and conversion devices such as batteries, supercapacitors and fuel cells. Through this work, we report the systematic development of a method to fully characterise the carbon porous networks using a molecular dynamics simulation testbed. Our work entails modelling and simulation of porous carbon structures using quenched molecular dynamics (QMD) simulations using Gaussian Approximation potential (GAP) and benchmarking the results with prior literature. This modelling technique can reliably be used for quantitative characterisation of the interconnectivity in porous structures to study ionic movements and charge transfer mechanisms. A new parameter, namely nearest neighbour search (NNS) coefficient was introduced to quantify homogeneity and networking in the porous structures. NNS coefficient increased from 1.62 to 1.92 with decrease of the annealing

temperature from 8000 K to 4000 K in carbon. The procedure outlined was although tested on porous carbon networks, but adaptable to study any other material system at multi-length scales.

Keywords: Molecular dynamics, Porous materials, Pore interconnectivity, Sphere pore model, Nearest neighbour search

1. Introduction

Carbon-based materials such as activated carbon, carbon nanotubes, fullerene, graphene, carbon aerogel etc. are ubiquitous to fabricate post-Moore's law engineering components to drive newly emerging requirements in the area of energy storage, energy conversion, catalysis, electronics and many more. Porous carbon materials by virtue of their high surface area are also prime candidates for hydrogen storage [1] [2]. Tuneable porosity in porous carbon network is one of the key desirable properties as this can change the response of an electrode.

Porosity in carbon-based materials refers to pore cavities and the interconnectivity of the pores to ease the ion transfer mechanism. This in turn facilitates their adsorption which is an essential property to use porous carbon as electrodes in energy storage and conversion devices such as batteries with different chemistries (Li/Na/Mg etc.), supercapacitors, fuel cells, hybrids etc. [3]. Capacity of energy storage devices are greatly affected by the interconnected pores and the number of solvated ions that can transfer to and from the electrolytic solution during charging/discharging of the device [4]. The porous spaces are nested discontinuities in a solid matter [5]. As per the IUPAC, porous materials can be classified according to the size of the pores ($< 2 \text{ nm}$, $2 \text{ to } 50 \text{ nm}$, $> 50 \text{ nm}$) that constitute them, and the three main classes are micro-, meso- and macro- pores respectively [6].

Porous structures are generally bi-modal or multi-modal i.e., more than one class of pores can be present combining micro and meso-pores within the structure [7]. This makes them irregular and complex in their forms. Detailed insights into the pore architecture are extremely important in order to predict their behaviour during charge transfer which in turn provides a rationale to benchmark the device performance [8]. However, reliable techniques to characterise complex porous networks are extremely challenging, and limitations with existing methods to yield quantitative description of irregular pores is an impediment to de-novo design of energy efficient electrodes. The most important parameters that are usually required to characterise high energy density in energy storage and conversion devices include specific surface area (SSA), pore size distribution (PSD), pore volume (PV) and pore interconnectivity (PI) [9,10]. The most commonly used techniques used for characterising pore architectures include physisorption equilibrium isotherms of various gases such as nitrogen, argon or carbon dioxide adsorbates [11,12]. Brunauer-Emmett-Teller (BET) is one of the most commonly used gas physisorption methods for evaluating the SSA of pores [13,14]. However, BET can only provide global information on the extent of pore volume and this method overestimates SSA which renders the method unreliable [15].

Density Functional Theory (DFT) and Barrett-Joyner-Halenda (BJH) are exclusively used for estimation of PSD. Accuracy of DFT is much higher as compared to BJH [16]. X-ray micro-computed tomography (XCT) has also been used to capture insights into porous carbon structures of materials [17,18]. XCT scanning can provide information about the interfacial morphology and porosity of catalyst layers of carbon system [19]. All these methods can provide one or more parameters and the rest of the parameters are usually approximated through post processing of data. One of the most important parameters i.e., pores interconnectivity (PI) cannot be estimated using the existing techniques. For developing numerical models in batteries/supercapacitors, the

PI is termed as tortuosity that takes into account the transport of ions in the porous materials [20]. The tortuosity factor is generally considered to be a constant value; while the PI in an electrode changes across the junctions of connectivity.

Molecular dynamics (MD) simulations approach is widely used to model and investigate the feasibility of ion transport in electrodes and to study the formation of double layer/intercalation for charge storage, etc. [21,22]. Atomic-level studies can aid to reveal structure-property relations [23] with high fidelity. A number of simulation studies have been conducted to reveal the formation of porous structures based on different parameters. He et al. [24] investigated graphitisation mechanism during the thermal process and explained the dependence of temperature on the formation of pores. Bo et al. [25] used MD simulations to study the effect of doping on the specific surface area of an electrode which enhances the specific capacitance.

Bryant et al. [26–28] introduced a new approach based on swelling of spheres to characterise porous materials. Their method suggested that by assigning equal sized pores into the throats in the network can lead to inaccuracy in estimating pore connectivity [28].

Silin and Patzek [29] and Al-Kharusi et al. [30] developed methods to identify the largest spheres which could be inscribed within porous materials. However, the algorithm was computationally demanding. Bhattad et al. [31] studied the effect of pore density on the pore transportation. Their study identified that pore density affects the pore distribution and connectivity. Lombardo et al. [32] harnessed OpenPNM for performing modelling of the pore network with assistance of 3D porous geometries reconstructed from X-ray computed tomography (XCT) images.

A fundamental challenge in the field of network generation and modelling is the absence of a standard definition for non-uniform pores and their interconnecting throats in materials with

complex geometries. Moreover, the definition of pore morphology itself can differ, leading to the creation of different network structures for the same material. The lack of standardisation makes it very tough to identify which network model best represents the physical reality of a given porous material, adding to the complexity of the modelling process. This challenge is particularly pertinent when considering applications in energy storage and conversion devices, such as porous electrodes in electrochemical energy storage devices. Achieving a more precise and standardized approach to pore network characterisation can facilitate the development of electrode materials with enhanced energy storage and conversion capabilities, ultimately contributing to the advancement of clean energy technologies.

In this work, we focus on developing a generic algorithm to quantitatively describe the pore channels in an electrode for applications in energy storage and conversion devices which can suitably be used as a criterion to screen ionic movements during charge transfer. The algorithm reported here is fully transferable to quantify the pores and ligands to investigate other porous materials including metallic foams for a wide range of engineering applications. The wider benefit of this method will facilitate the development of post-processing MD softwares such as “OVITO”, “VMD”, “AtomEye” to name a few. During the course of investigation, efforts were made to systematically explore the use of quenched molecular dynamics (QMD) simulations to develop a sphere pore model for detailed characterisation of pore architecture and interconnectivity. Unlike previous studies, this iterative method generates an exclusive sphere pore model for given annealing conditions. Nearest neighbor search for identifying throats and the throat aspect ratio for assessing their quality were introduced. These parameters facilitated the examination of throats and offer a computationally inexpensive approach for quantifying the degree of homogeneity and networking within porous structures. Our developed sphere pore modelling technique can help to

identify the interconnectivity of the pores to better understand the migration of ions during the charging and discharging process. To quantify the robustness of our proposed method, we performed two case studies: (i) we compared performance of our model with previously reported model in the literature [33] by obtaining pore specific information in a carbon network and (2) we simulated the BET method to analyse the surface area of the simulated porous carbon to benchmark our results against the published experimental literature.

2. Simulation methodology

2.1. MD modelling

2.1.1 Potential energy function

An interatomic potential or a force-field refers to the mathematical rule governing the interactions between the carbon atoms. The potential for a material with a highly ordered and crystalline structure may be different from a material with a more disordered and amorphous structure. In our previous study [34], we used an adaptive intermolecular reactive empirical bond-order (AIREBO) potential [35]. A more recent formulation, namely, the Gaussian Approximation Potential (GAP) is a more general-purpose potential [36,37]. The recently developed GAP variant from Deringer and Csányi [38] can suitably describe the interactions in liquid and amorphous carbon with accuracy matching to DFT as it employed a kernel-based machine learning algorithm.

To test the transferability of a carbon potential, the simplest method is to establish the linear relationship of sp^3 or sp^2 fraction of carbon atoms in a system with respect to the density of system [39] [40]. To screen the two potentials, namely, AIREBO and GAP, we performed test simulations to compare their performance for low density amorphous carbons (0.5 to 2 g/cm³) against the published experiments and the results are summarised in **Fig. 1**. We noticed that at low density of

0.5 g/cm³, both potentials showed comparable sp^3 fractions but as the density of the system increases to about 1.75 g/cm³, significant deviations can be seen. For a density of 0.95 g/cm³, the sp^3 fraction revealed by GAP was 64.2% higher than the AIREBO potential. Furthermore, this comparison highlighted that the GAP potential showed higher sp^3 fraction values than the AIREBO potential in the density range of 0.5 to 2 g/cm³. This trend was in good qualitative agreement with the experimental [41] and DFT data [42,43]. Experimental results of Schwan et al. [44] compared and shown in *Fig. 1* reinforce the argument that the GAP potential achieves better accuracy than the AIREBO potential for modelling of low density amorphous carbon system. For these reasons, this work used GAP interatomic potential for performing the QMD simulations at three representative temperatures as an extended effort to the previous preliminary work [34]. Further, we study patches of graphitic-like ribbons obtained from the GAP-quenched structures and disordered sp^2 network at different temperatures. As for the BET adsorption simulation, we used an LJ potential scheme to describe the nitrogen-carbon interactions with the force-field parameters shown in **Table 1**.

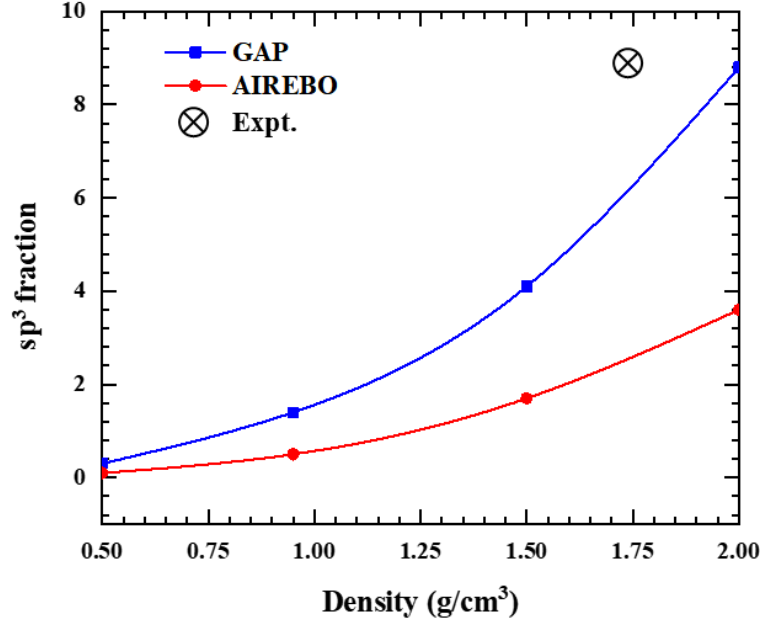


Fig. 1: sp^3 fraction vs. density plots for AIREBO and GAP interatomic potential

Table 1: LJ potential used to perform the BET test

Interaction type	LJ parameters
C-C interactions	$\sigma = 0.34$ nm and $\epsilon/k_B = 32.9$ K [45]
N-N interactions	$\sigma = 0.375$ nm and $\epsilon/k_B = 95.2$ K [45]
C-N interactions	$\sigma = 0.336$ nm and $\epsilon/k_B = 61.4$ K [45]

2.1.2 MD simulation parameters

LAMMPS simulation package (version 24-Mar-2022) [46] was used to perform the QMD simulations. A fixed cuboid of dimension $20.3 \text{ nm} \times 10.1 \text{ nm} \times 10.1 \text{ nm}$ containing 100,000 carbon atoms at a density of 0.95 g/cm^3 with periodic boundary conditions was used to simulate the system. All computations were performed with a timestep of 0.5 fs. For maintaining a constant temperature during the simulations, we used the canonical ensemble (NVT) [47]. The initial

temperature of the system was maintained at 10,000 K to reduce any bias that may come from an ordered initial state. This method yielded a carbon system with a fluid-like behaviour and assisted in randomly displacing the atoms within the system. From 10,000 K, the system was cooled to 300 K at three different quench rates based on the type of porous structure required. We employed an annealing methodology that mimics the experimental synthesis of TiC-CDC [48] wherein we maintain the temperature at a constant value for a considerable amount of time during simulations. The carbon system was annealed for 30 ps at temperatures of 8000 K, 6000 K and 4000 K to form three porous carbon systems, namely AT8000, AT6000 and AT4000 respectively. This annealing procedure was critical for transitioning from a high-energy quenched structure to an equilibrated relaxed structure. The results from intermediate quench rates employed to form various carbon systems are provided as supplementary information (see *Fig. S1*). OVITO software was used for postprocessing of the simulated results [49]. Nearest neighbour count was performed to gather the information about the sp , sp^2 , and sp^3 structural motifs using a cut-off distance of 1.735 Å for hexagonal ring bonds, which fully encloses the first-neighbours shell for porous carbons [50]. Furthermore, to study the graphitic ribbon, radial function distribution (RDF) analysis was carried out.

2.2 Porous structure characterisation

To estimate SSA and PSD, BET and DFT methods use an idealised geometric model which neglects the interconnectivity of the pores, coordination and the heterogeneity of the porous network [51]. Such pore models may not be suitable for predicting diffusion rates as they provide qualitatively incorrect heat of adsorption [52]. Knowledge of PSD is particularly important since it can determine whether the energy storage and conversion devices will be high energy

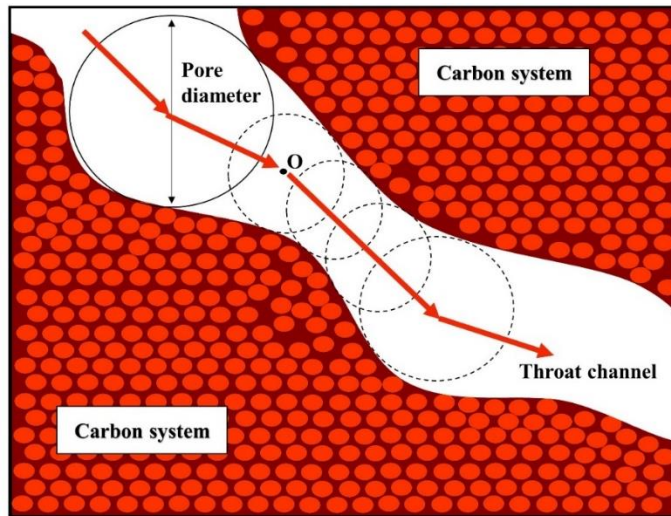
(microporous) or high power (meso & macro-porous) devices. The current limitations arise from the accurate analysis to arrive at the PSD which is computationally demanding. In this subsection, we outline a systematic process for estimating the PSD in an effortless manner.

2.2.1 Sphere pore model

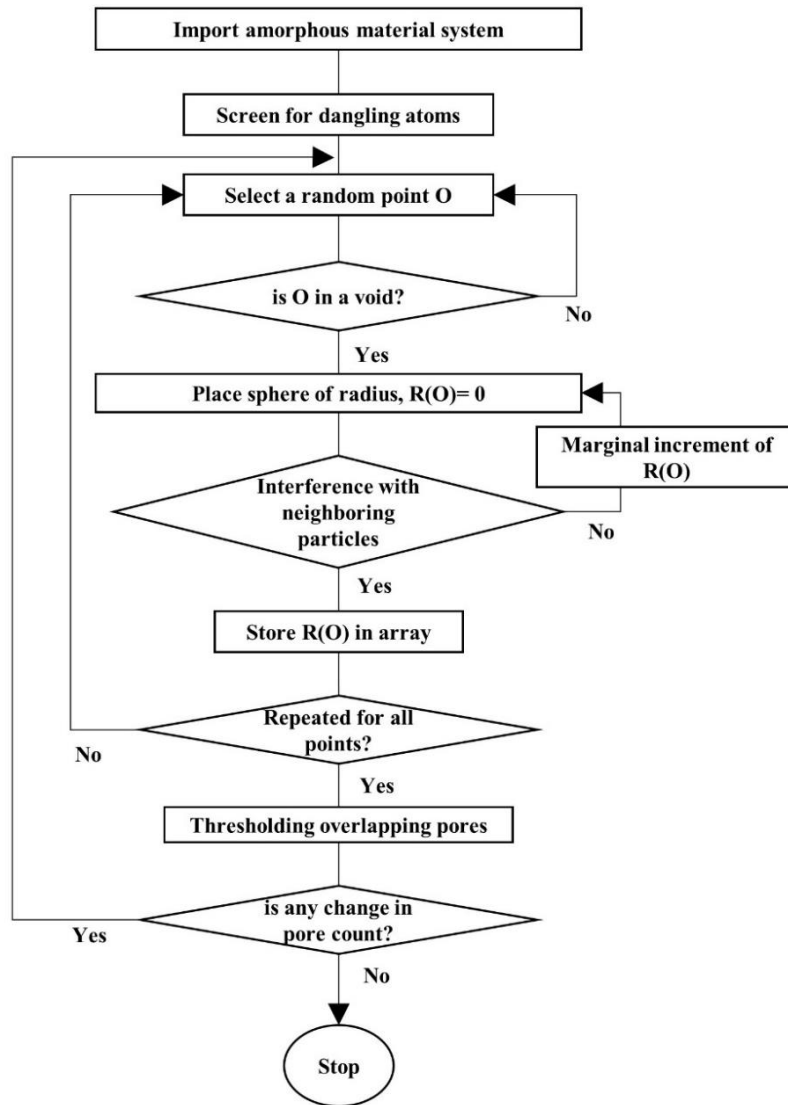
One particular assumption considered while developing this model was that the boundary of pores is always in the shape of a curve that will fit a sphere of varying diameter depending on the size of the curvature of the pore boundary. The pore size at any location in the structure is defined as the largest sphere that can accommodate the pore without overlapping with the neighbouring atom. *Fig. 2 (a)* show a 2-D schematic illustration. The dotted circles are different sized spheres that can be constructed through a pore channel. The proposed approach is explained through a flowchart in *Fig. 2 (b)*.

The first step in this approach involves the creation of evenly distributed points separated by bond length of carbon in the entire structure (including the solid part). The next step involved removal of points overlapping with C-atoms (solid part). This leaves a database of all possible points forming the pores in entire structure. Thus, each point was considered as a centre to form a sphere around it. The size of the sphere was increased until the periphery of the sphere touches the pore boundary. This step continued until all points forming the centre of spheres touched the pore boundaries. A point closer to the pore boundary created a smaller sphere whereas a point far away from the pore boundary created a large sphere. Additionally, a database of all possible spheres overlapping with each other was also created; one of the key criteria was that the diameter of the sphere shall not exceed 0.154 nm because a typical carbon hexagonal ring has a side length of 0.154 nm and a central void space to fit a sphere of diameter 0.154 nm [53]. Once the database

containing radius, centre and coordinates of all possible spheres was created, the next step was to rank the spheres in order of their decreasing radius. Starting from the largest sphere(s), all other spheres overlapping with it were removed. Subsequently, the second largest sphere(s) was considered and all possible spheres overlapping it were deleted. This iteration continued until the porous structures had all possible non-overlapping spheres with varying radii. This process yielded a configuration with partial filling of the porous structure with spheres. Subsequently, an iterative method was adopted such that the entire process was repeated starting from the creation of evenly distributed points until the formation of non-overlapping spheres. These iterations were carried out until no new spheres were left. The final result was an array of non-overlapping pores which completely filled the void space in the carbon system. The pore size distribution for different cases of carbon systems were calculated by the radii of best-fitted sphere pores.



(a)



(b)

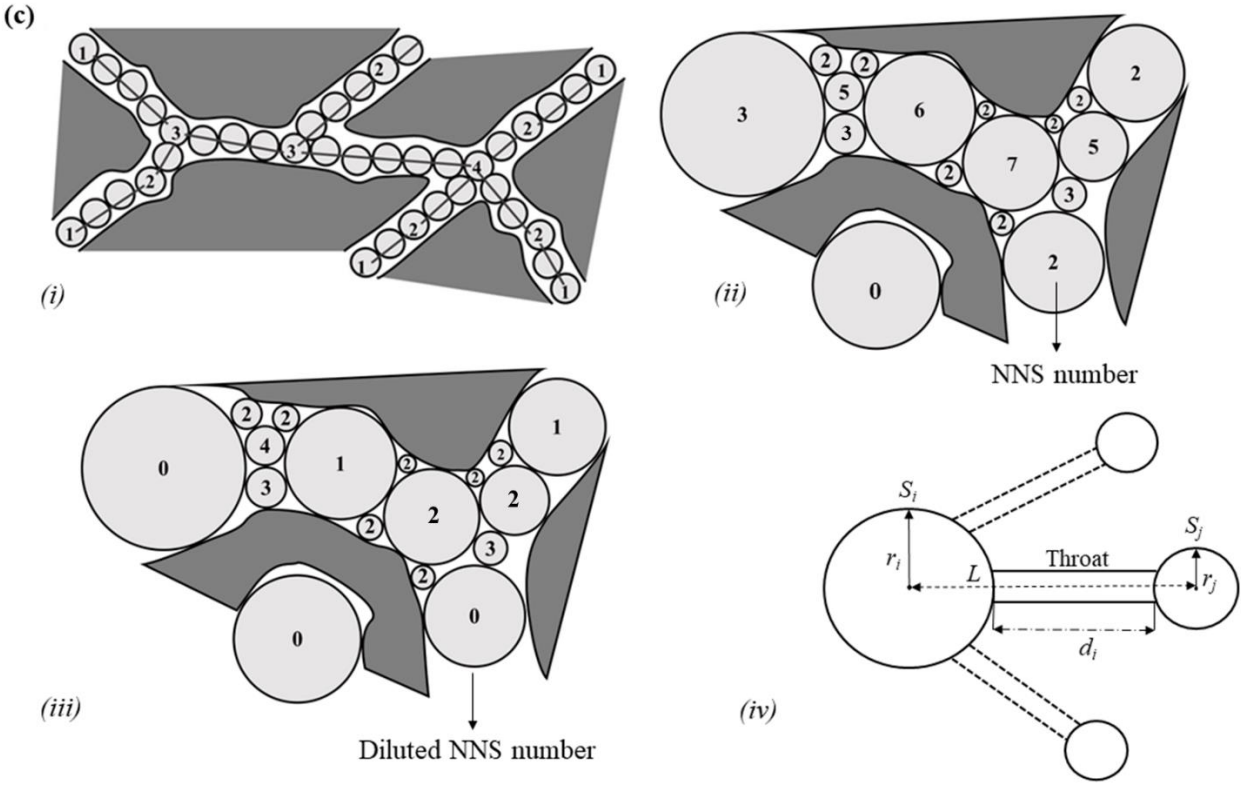


Fig. 2 (a) Schematic for sphere pore fitting across porosity of carbon system, (b) Proposed procedure to count the number of spherical pores. Here, O is a random sampling point inside the model volume, $R(O)$ is the particle radius, respectively. (c) 2D representation of a system of sphere pore model with assigned NNS numbers for different neighbour throat possibility (i) Ideal case of uniform pore channel cross sectional area and shape, (ii) Realistic case with varying pore channel cross sectional area with NNS number, (iii) Realistic case with varying pore channel cross sectional area with diluted NNS number, (iv) A schematic showing a sphere connected to other spheres using throats. L indicates the centre-to-centre distance between the spheres; d_i indicates the size of throat; r_i and r_j indicates the radii of the spheres S_i and S_j .

2.2.2 Near neighbour search (NNS) study

Complex pore structures can be reproduced using an equivalent pore network model of PI [54]. Pore network model simplifies the porous structure into pores and throats. Such models usually approximate pores and throats as spheres and cylinders respectively in order to analyse the

pore network [55]. Such a pore network extraction algorithm helps in overcoming the limitations posed in conventional network modelling predictions wherein the complex pore structures are oversimplified.

In this study, pores and throats were identified using NNS analysis of the sphere pore model. NNS analysis can provide an accurate representation of the degree of interconnectivity in the porous structure. The NNS number of a pore represents the number of different pore spheres connected to a pore. An ideal model with uniform cross-sectional pore channels after the application of the sphere pore model would contain pore spheres of uniform radii packing the entire void space. A 2-D representation of this is shown in **Fig. 2 (c)**. In such a case, each sphere will have a certain NNS number, i.e., the number of connecting spheres directly connected to the node. Spherical pores located at the middle of a channel would be surrounded by two other spheres, one in front and the other at the rear. Hence, the NNS number for this middle pore is two. A similar sphere situated at the junction of multiple channels would be connected with a higher number of spheres. The sphere at the junction, mentioned here onwards as a node, has NNS number equal to the number of coinciding channels. **Fig. 2 (c) (i)** explains this concept with few examples. Spheres numbered two are situated in the middle of a channel, whereas spheres numbered otherwise are at junctions for as many channels. A database of an ideal case involving the NNS data for all pores provides an excellent approximation of the degree of connectivity in the porous carbon.

However, a real system contains pore spaces which are uneven in their cross-sectional area. Such a system would contain pore spheres of varying radii (**Fig. 2 (c) (ii-iii)**). Determining the NNS number in such a case is not straightforward. To extract NNS number for real systems, a sphere (S_i) surrounded by spheres of varying radii (let one of the spheres be named S_j) (**Fig. 2 (c)**

(iv)) was assumed. The number of throats connecting S_i with all its neighbouring spheres determines the NNS number of S_i . The throat size (d_i) can be found using the following conditions:

$$d_i = L - (r_i + r_j) \quad (1)$$

$$d_i < 0.154 \text{ nm} \quad (2)$$

Throat size ≥ 0.154 nm for two spheres indicated the presence of a single/multiple graphitic sheet present between the pores and therefore, removed from calculations. Using these conditions, the NNS number for each sphere in **Fig. 2 (c) (ii)** was calculated. A sphere assigned NNS number of X indicates that X neighbouring spheres are connected to it through its boundary. However, NNS number will not provide information on whether the ions moving in the porous network will have higher diffusion rates e.g., a large sized pore (higher charge storage) connecting to a smaller sized pore will lead to reduced diffusion rates since ions filling the larger pores will take longer to move through the network due to non-availability of space in the next sphere. For higher diffusion rates in the porous network, it is imperative to have PI such that a pore (or sphere) is always connected to an adjacent larger or comparable sized pore (or sphere). Due to this, the development of a diluted NNS number is required to ascertain the PI with higher diffusion rates. For this, an iterative method was adopted with three conditions in decreasing order of priority to determine the diluted NNS number.

i) Choosing the throat with a higher priority defined by the following formula:

$$P_{ij} = 1 + f(S_i) \times f(S_j) \quad (3)$$

$$f(S_i) = 1 - \frac{n_i}{a_i} \quad (4)$$

where P_{ij} : significance of throat that joins S_i and S_j , n_i : NNS number of sphere S_i , a_i : available number of connections for sphere S_i .

ii) Choosing the throat with the smallest length.

iii) Choosing the throat which interlinks the sphere with a comparable or larger sized sphere.

Through this the diluted NNS number was calculated. **Fig. 2 (c) (iii)** show the diluted NNS number of each sphere. A sphere with a higher NNS number contributes to higher diffusion rates leading to higher power density while a sphere with a lower diluted NNS number contributes to higher charge storage leading to higher energy density.

2.3 Adsorption isotherm analysis

An atomistic modelling used for nitrogen adsorption isotherm [56], and the obtained data was post-processed to calculate the SSA of the porous carbon structure. Nitrogen gas (adsorbate) at 77 K was routed through the carbon system. In the process, nitrogen was adsorbed onto the surface of the porous carbon structure because of interactions between carbon atoms and nitrogen molecules, resulting in multilayer nitrogen gas adsorption over the porous carbon structure. Once the nitrogen adsorption over the porous carbon structure completes, the BET surface area was calculated using the monolayer of nitrogen that was adsorbed into the surface of the porous carbon. The BET surface area was estimated as:

$$A = N_m \times A_c \times N_{av} . \quad (5)$$

where A is the BET surface area, N_m is the monolayer of nitrogen adsorbed (number of molecules), A_c is the cross-section of the adsorbate (16.2 \AA^2 for N_2) [57], N_{av} is the Avogadro's constant. The adsorbed monolayer of nitrogen was calculated using the BET equation [58] as:

$$\frac{\frac{P}{P_0}}{N \left[1 - \left(\frac{P}{P_0} \right) \right]} = \frac{1}{N_m \times C} + \frac{C-1}{N_m \times C} \left(\frac{P}{P_0} \right). \quad (6)$$

where $\frac{P}{P_0}$ is the relative pressure with $P_0 = 1$ bar, N is the total number of molecules of nitrogen adsorbed, and $C = 1 + \frac{\text{slope}}{\text{intercept}}$ is the BET constant.

3. Results and discussions

To generate atomistic models of the porous carbon structures, we adopted a QMD routine [59]. The quenching temperature was made to vary from 10,000 K to 300 K with varied annealing temperatures and the thermal responses were obtained from the simulations (shown as supplementary in *Fig. S2*). *Fig. 3 (a)* compares the simulated structures for three different annealing temperatures used (Case 1 – AT8000, Case 2 – AT6000 and Case 3 – AT4000). A comparison of image insets of *Fig 3 (a)* show that the carbon mesh becomes denser with increasing annealing temperature. At a higher annealing temperature of 8000 K, the simulated structure was seen to be comprised of relatively small and uniform pores. The curved structures were seen in the case of an annealing temperature of 4000 K, and larger pores begin to develop. For cases 2 and 3, the graphitic ribbons were long and straight compared to case 1. For case 3, the simulated carbon structure formed stacked graphene nanosheets. However, stacking was absent in cases 1 and 2. The results complement the previously reported experimental work (TEM) as well as the simulation work reported by Tomas et al. [59].

Our simulation strategy of annealing at different temperatures for 40 ps was adopted to mimic the experimental temperature of 1800 K. It is good to note an excellent agreement between the simulation results and the previously reported experimental results that reproduced large stacks of graphitic ribbons [59].

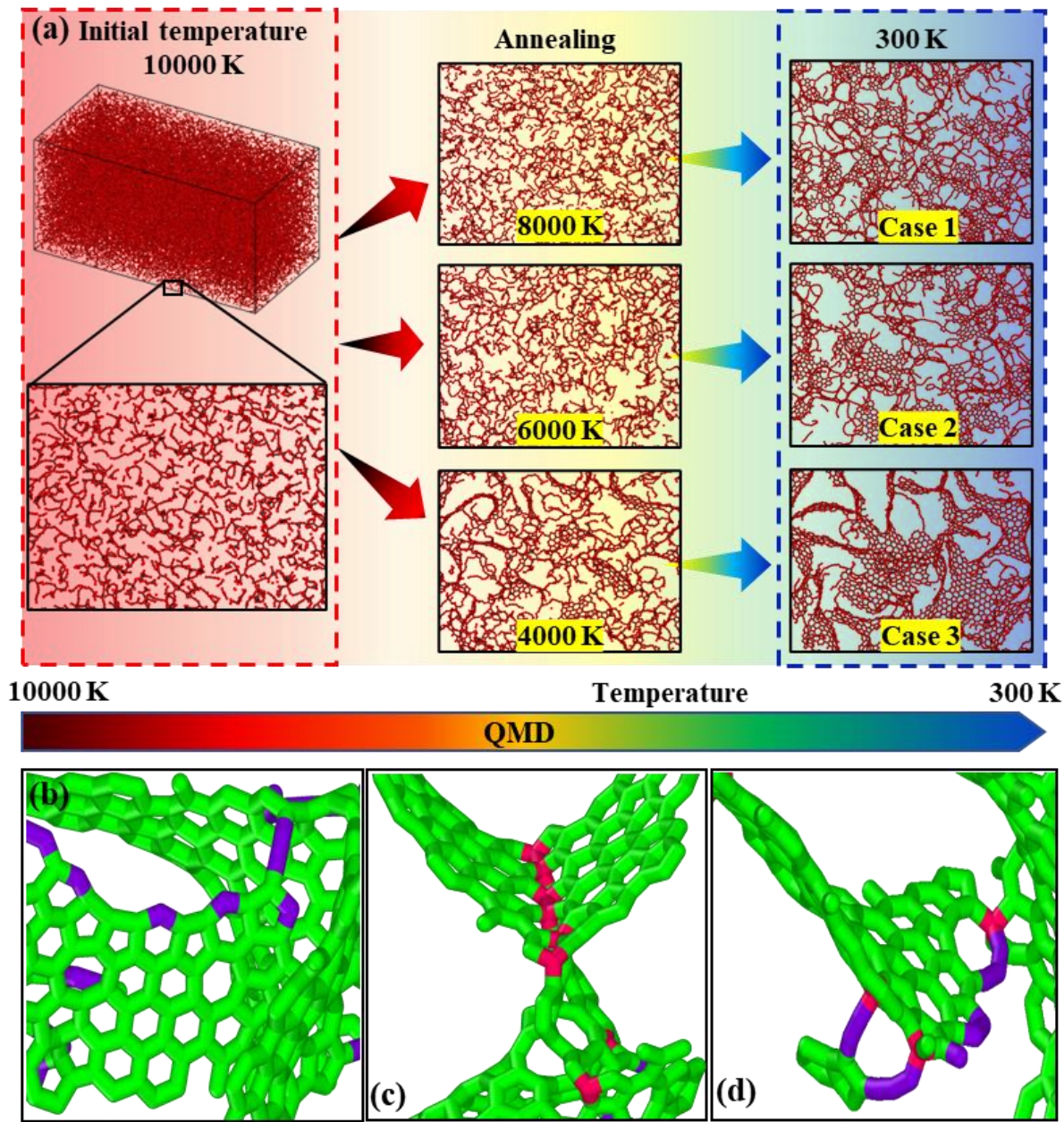


Fig. 3 (a) Carbon systems obtained for different annealing temperatures (b-d) representation of sp^n ($1 \leq n \leq 3$) motifs in C-C bonds: (b) sp motifs, (c) sp^3 motifs, and (d) combined sp and sp^3 motifs for AT4000.

3.1 Analysis of carbon structures

For qualitative validation of honeycomb nanostructure formations, we studied the cross-sectional morphology of structures corresponding to annealing temperature of 4000 K (*Case 3*)

(**Fig. 3 (b)**). It can clearly be seen that the structures mostly comprise of curved graphene fragments with sp^2 bonding as being most prevalent. **Table 2** provides quantitative analysis for all the three cases simulated in this study.

Table 2. Fractions of sp^n ($1 \leq n \leq 3$) bonds, NNS number coefficient, throat aspect ratio, and BET surface area obtained for different annealing cases.

Parameter	sp^n ($1 \leq n \leq 3$) fraction (in %)			NNS number coefficient	Throat aspect ratio	BET specific surface area (m^2/g)
	sp	sp^2	sp^3			
Case – 1 (AT8000)	30.3	68.4	1.3	1.62	1.172	464.0
Case – 2 (AT6000)	28.2	70.0	1.6	1.66	1.172	906.7
Case – 3 (AT4000)	12.3	86.4	1.3	1.92	1.148	1485.0

The small fragments were observed to link together to form an interconnected geometrical complex network, with edges containing sp motifs and planes to be interconnected by using the sp^3 motifs (refer **Fig. 3 (b-d)**). This observation was analogous to the interstitial defects that are present in carbon-based materials (in this case graphite). Another feature that was identified from the interconnected network was the nanoscale arrangement of differently tangled graphitic ribbons, as shown in **Fig. 3 (b-d)**. A detailed study about the pore morphology is presented in the later sections. With respect to the extremely significant sp^2 fraction as shown in **Table 2**, the observed outcomes indicated predominance of the hexagonal ring motifs in the porous structure. It was also observed that a fraction of unstable defective rings remained present for all the cases studied here. It was seen that the graphitic ribbons were stacked in AT4000 as shown in **Fig. 4 (a)**. Various structural parameters were calculated to study and ensure the stability of the developed structures. These features were compared to the experimental data from the published literature.

Characterisation of the experimental and computational porous structures using the radial distribution functions, $g(r)$ is discussed next.

$$g(r) = 4\pi\rho_{at}[g(r) - 1] \quad (7)$$

where ρ_{at} is the atomic density in atoms/Å³

Fig. 4 (b) depicts the $g(r)$ of the control experimental data and carbon samples simulated in this work. Based on the similarity with the mass density, 0.95 g/cm³ was chosen to be the closest to carbide-derived carbon (CDC) models [60]. As a result of the scaling process, oscillations remained, but its intensity decreases as the radius (r) increases.

Fig. 4 (b) show the enlarged initial three peaks of the carbon sample spectrum. For all the simulated structures, the distance between the six-membered ring was similar to the indicated three initial peaks. These three peaks are represented as a , b , and c , where the distances they represent relates to the interatomic distances within a six-membered hexagonal ring of carbon. These peaks provide an idea about the defect free graphitic areas in the structure (i.e., made of hexagonal rings only). It was also observed that the relative intensities of peaks for all cases in this study are similar to the experimental $g(r)$ spectra of CDC shown by Thompson et al. [61]. The initial three peaks at 1.42 Å, 2.52 Å and 2.87 Å represents neighbours in a hexagonal ring and peaks at 3.77 Å, 4.32 Å, and 5.02 Å represents the location of carbon atoms in the neighbouring rings. However, non-hexagonal rings were also present in the struts as indicated by the asymmetries in the peaks after the initial three. It was observed that the reduction in the annealing temperature caused an increase in the intensity of peaks and reduction in peak broadening. This could be due to the presence of higher level of impurities at higher annealing temperature samples. It brings defects within the hexagonal crystallinity of graphene nanosheets, which could effectively lower the medium-range order. In this sample, the graphitic sheets were stacked locally like a graphite crystal encompassing

multi-layers, as shown in **Fig. 4(a)**. The results obtained here were in close proximity with the results published by Shiell et al [62] using Raman and TEM analysis.

Next, a quantitative characterisation for pore volume, PSD and pore interconnectivity is presented followed by the BET analysis for estimation of the SSA.

3.2 Sphere pore analysis

Characterisation of pores and the porous architecture through our developed sphere pore model forms the crux of this work. **Fig 5 (a)** shows the partial carbon system for the case when the annealing temperature was 4000 K (AT4000). This system was further subjected to the proposed sphere pore method as already discussed in the *previous section*. Grey spheres represent the pores of best fitting size. Applying this method, we found that the structures yield a porosity of about 20.4% for AT8000 and 25.6% for AT4000. In carbon systems, voids between stacked graphitic ribbons led to the formation of micropores (refer **Fig 3 (a)**).

Pore size distributions for different annealing cases are shown in **Fig. 5 (b)**. A unique observation from the histograms shown was that only the AT4000 sample showed pores with relatively larger pore diameter > 1.5 nm. In general, these results are consistent with previous studies where pore size and dispersity increases with the rate of quenching [63]. PSD graphs showed the demarcation of pore sizes at different annealing temperatures. Although all three cases show mostly microporous distribution i.e. pore widths < 2 nm, their application as high energy storage devices largely depend on the corresponding ions size in the electrolytes. The maximum capacitance attainable in supercapacitors is ideally the case when the pore size is almost equal to the ion size [64], assuming no ion crowding. This is because of the strong electrode atom (say positively charged) – ion from electrolyte (say negatively charged) interaction that repels other

similar ions (negatively charged) near the pores, thereby allowing only single electrode atom – ion double layer formation. In case the pore size is larger than the ion size, capacitance will be lower due to multiple ions accumulating in the pores, thereby reducing the strong interaction between the electrode atoms – ions (similar charged ions will be repelling each other). On the other hand, if a pore size is smaller with respect to the ion size, then the ions will not be able to move inside the pores, thereby treating the pores as flat surfaces. This will greatly reduce the performance of the overall device. Therefore, an optimal PSD is extremely necessary for obtaining high energy density devices.

The mean pore diameters for different cases were 0.48 nm, 0.49 nm and 0.51 nm for the three cases respectively. A small shoulder from 1 to 1.1 nm particularly for *case 3* represent the largest pore which was located between stacked graphene layers at lower annealing temperatures. Therefore, increase in the mean pore diameter along with graphitic ordering was consistent with the current discussion. These results highlight the effectiveness of the proposed method in characterising the pore space and revealing the effects of underlying structural changes.

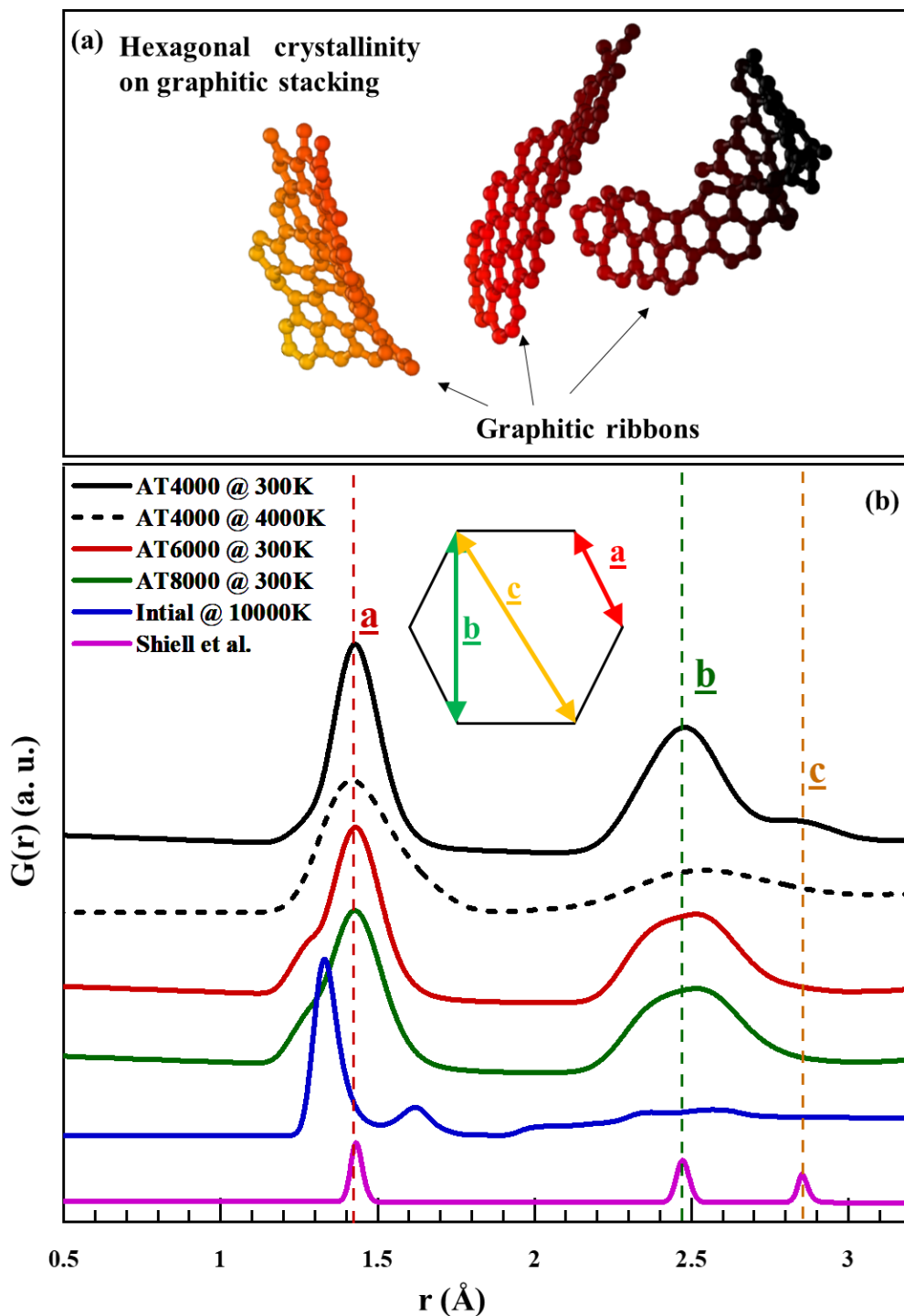


Fig. 4 (a) Hexagonal crystallinity obtained for various stacks of sp^2 ribbons (*light to dark colour coding from left to right is provided for better visibility or overlapping rings of carbon*); (b) Reduced RDF analysis for different annealing cases, here, inset show the significance of a , b , and c peaks for the formation of hexagonal rings compared with standard and experimental graphs reported by Shiell et al. [62].

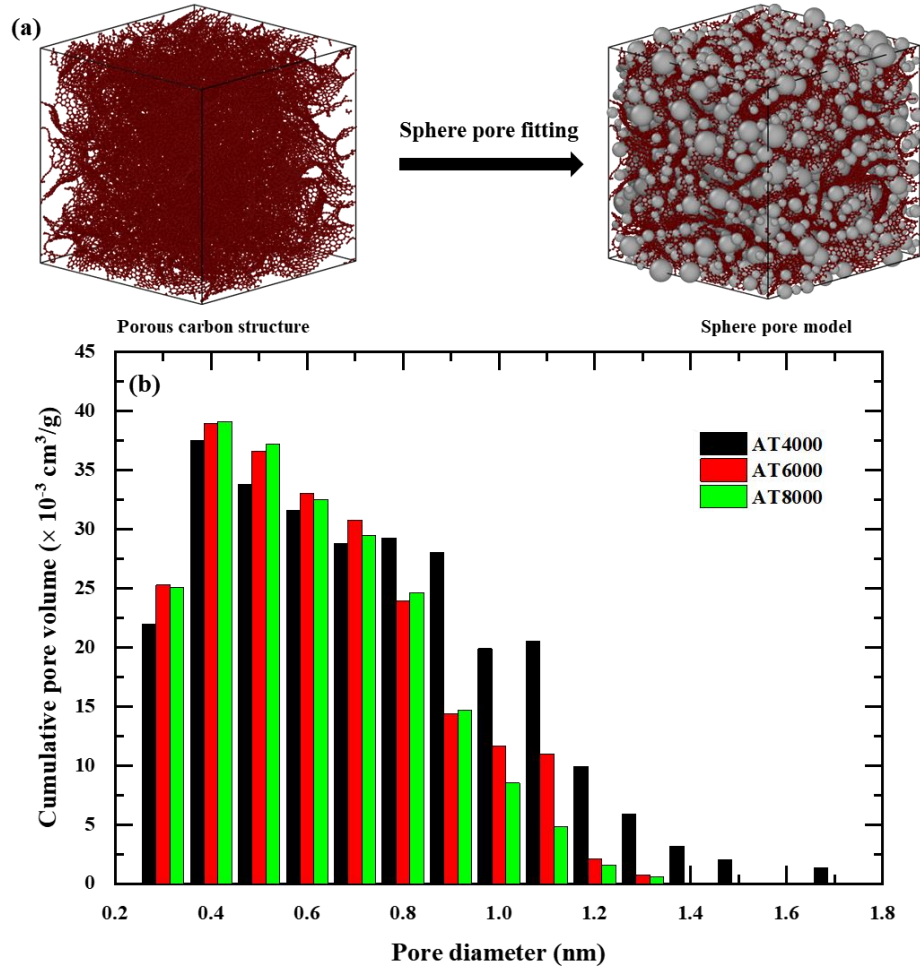


Fig. 5 (a) Sphere pore filling model for the AT4000 carbon system, (b) PSD graphs for different annealing cases

3.2.1 Pore network analysis

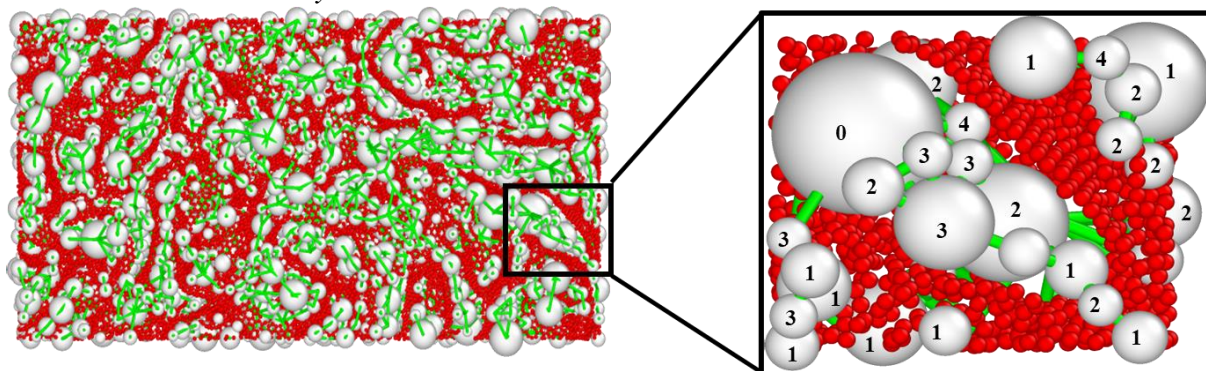


Fig. 6 Diluted NNS number analysis for AT4000 carbon system. Red and white spheres represent carbon atoms and pore spheres respectively. Green bonds depict throats between two pore spheres (inset shows the magnified view of selected pores with their diluted NNS number).

NNS number can provide information about the transport properties within the porous structures such as the diffusion coefficient [55]. NNS number can be obtained by calculating the number of throats directly connecting the pores to their corresponding neighbour pore bodies. A higher value of NNS number indicates high degree of PI i.e., pores are well connected to each other. This indicates high tortuosity and increased diffusion [65]. We adopted a strategy to calculate diluted NNS number to further find the PI with varying sizes that contributes to higher energy or power density.

Fig. 6 depicts the diluted NNS number of pores within a sliced section of AT4000. The carbon atoms are represented as red spheres, pores of different diameters are shown with white spheres and throats as green bonds. The inset alongside shows a magnified view of the fitted pores and throats with calculated diluted NNS numbers for each pore.

Fig. 7 (a) presents the diluted NNS number distributions and mean diluted NNS number of three carbon samples. The distribution of the calculated diluted NNS number vary from a minimum of 0 to a maximum of 8. AT4000 showed a mean diluted NNS number value of 2.08, which is largest among the three annealing cases. The mean diluted NNS number of AT4000 was 15.3% higher than the AT8000. The distribution of radii for each individual diluted NNS number is shown in *Fig. 7 (b)*. The graph extracted for the three carbon samples, each containing total pores ranging from 5153 for AT4000 to 5461 for AT8000 with varying diameters. It is evident that the larger pores have lower diluted NNS numbers, whereas smaller pores dominate the curve for larger diluted NNS numbers. AT4000 showed highest peaks for all diluted NNS numbers larger than 2 compared to AT6000 and AT8000. It is evident from the NNS analysis that pores participating in the network channels had higher diluted NNS numbers.

Wider interconnected throats facilitated higher permeability in a porous carbon system. Size of throat is directly proportional to the diameter of its associated pores. Thus, the NNS coefficient was calculated to estimate the weightage of pore diameter in NNS analysis. A weight factor is associated with pore radius to interpret the true connectivity with a particular carbon sample. NNS coefficient is a promising way to quantify network structures in the carbon samples. It is a weighted average of diluted NNS numbers for all the pores. The NNS coefficient was obtained by characterising pore connectivity as:

$$\zeta = \left(\frac{1}{N} D_{avg}\right) \sum_i (C_i \times d_i) \quad (6)$$

where N is the total number of pores, D_{avg} is the average diameter of pores, C_i and d_i are the diluted NNS number and diameter respectively for pore i .

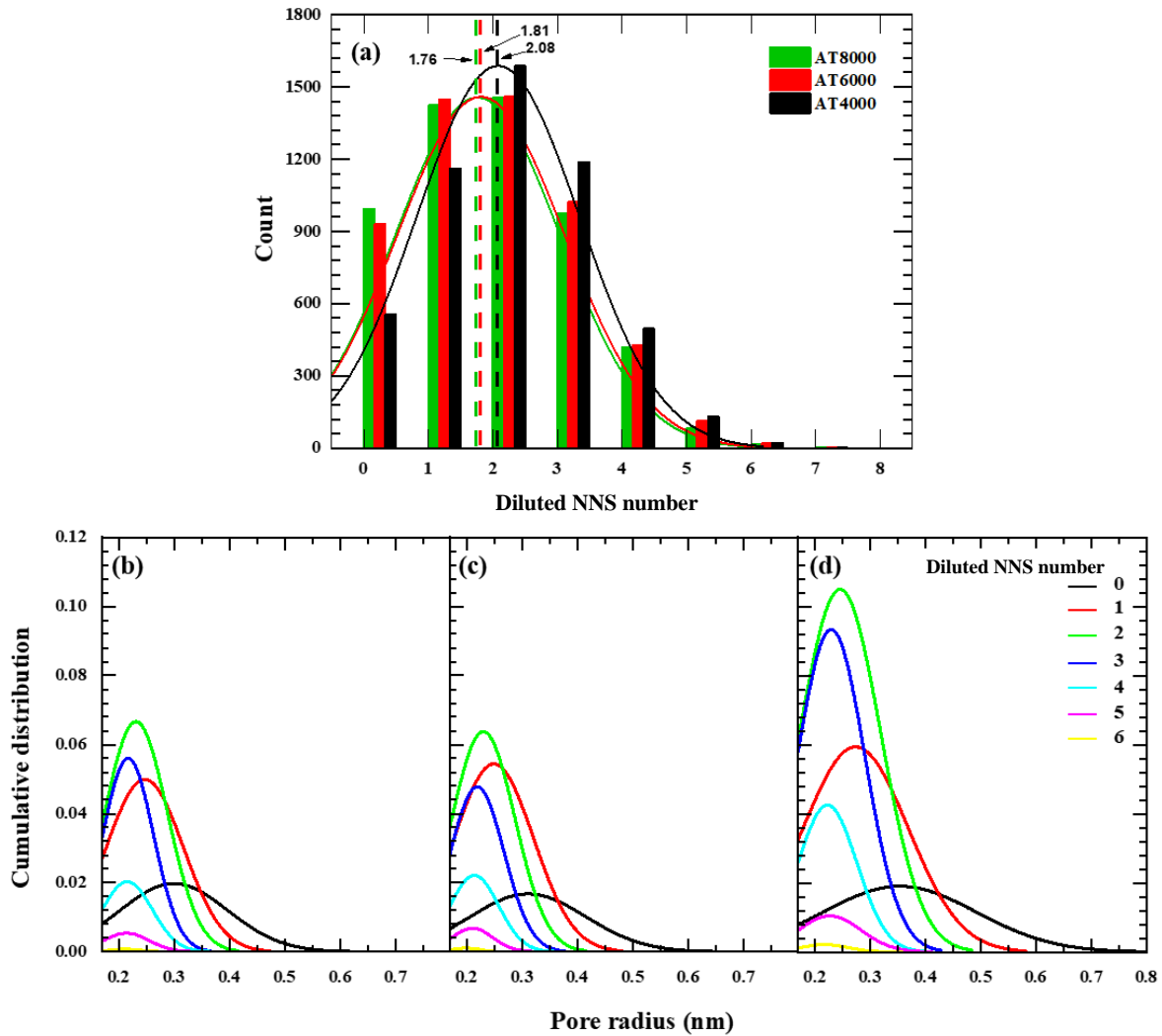


Fig. 7 (a) Diluted NNS number distributions and the mean diluted NNS number of the three carbon samples. (b-d) Cumulative distribution of sphere pores as a function of pore radius for each diluted NNS number. (b) AT8000, (c) AT6000 and (d) AT4000.

NNS coefficient compared earlier in *Table 2* for all three carbon systems showed noticeable changes in the NNS coefficient for AT8000 (low porosity) and AT4000 (high porosity). One can see that the AT4000 revealed the largest NNS coefficient of 1.921, indicating that the PI for AT 4000 was largest compared to the other cases. AT8000 showed least NNS coefficient of 1.629 which can also be verified by a low porosity of 20.4% as compared to 25.6% for AT4000. Low NNS coefficient is an indicator of low connectivity that may be due to two adjacent pores

separated by solid structures instead of throats. This parameter can be taken as a qualitative indicator for diffusion of ions during charging and discharging for energy storage and conversion devices as higher diffusion is possible when throats are present in the porous structures. Low NNS coefficient will lead to ions getting stuck in the pores without any throats thereby leading to slow diffusion during charging and discharging. This indirectly affects the power density of the devices [66]. Additionally, the PI for the three porous carbon structures were further investigated using electrolyte transferability through the structures by using EMIM BF₄ electrolyte as reference case study. From this study, it was observed that the AT4000 structure swiftly passed a large number of EMIM BF₄ ions through the structure compared to the AT6000 and AT8000 structures. This electrolyte transferability through the AT4000 carbon structure is shown in the supplementary data (*Fig. S3 – S4 and supplementary video*). Detailed analysis on ion transferability through the porous structures will be discussed in a follow on study of this work.

3.2.2 Throat aspect ratio (TAR)

TAR provides information on the degree of homogeneity of the porous structure [67]. We do not claim to develop this new parameter, but we simply used this parameter to check the robustness of our MD simulation system.

Global aspect ratio (GAR) indicates the ratio between the average of the two pore sizes that shares a throat and the length of the corresponding throat. The average TAR (τ) was calculated based on the equation:

$$\tau = \left(\frac{1}{N}\right) \sum_k \left(\frac{L_k}{D_{mean}}\right) \quad (7)$$

where the length of throat k is denoted by L_k and the average diameter of the two pores connected to throat k is denoted by D_{mean} .

This study used TAR to analyse the differences pertaining to the dimension of pores and throats. As shown in **Table 2**, TAR ranges from 1.148 to 1.172 for AT4000 and AT8000, respectively. Compared to AT4000, the AT8000 samples showed a higher TAR, indicating that there were pores that may exist in the form of bottlenecks. Higher value of TAR for AT8000 is also an indication of poor connectivity in porous carbon structures.

3.3 BET adsorption isotherm analysis

In BET adsorption isotherm process, the relative pressure (P/P_0) of the adsorbent (here, nitrogen) is directly related to their adsorption on porous carbon structure [68]. Thus, analysing the BET adsorption isotherm aids in calculating the surface area of the porous carbon structure in relation to the adsorbed volume of nitrogen inside the structure. The BET adsorption isotherm result is shown in **Fig. 8**. The BET adsorption isotherms of this study are in good agreement with the experimental reported results of Lee et al. [68] and Mistar et al. [69].

From the MD simulation of BET surface area analysis of porous carbon structure, it was observed that when nitrogen gas passes through the porous carbon structure, initially the nitrogen formed a monolayer (a single layer of nitrogen molecules) on the walls, and as the pressure of the nitrogen increases gradually, the volume of nitrogen filling the porous structure increases, leading to the formation of multi-layered nitrogen (nitrogen molecules forming multiple layers one over the other) over the structure. Gradually, the porous structure gets filled with nitrogen, and the BET adsorption isotherm was obtained and plotted. In general, there are six types of BET isotherms available based on the shape of the plot, which in turn, represents the volume of adsorbent that was adsorbed into the porous structure [70].

In our simulations, *Type 1* isotherm was found, which showed that the porous carbon structure has micropores. This could be understood from the BET isotherm region, which corresponds to 0 to 0.2 relative pressure. Over this area, it could be seen that the amount of nitrogen that has been adsorbed by the porous carbon increases rapidly with pressure which resonates with the observations made by Khosrowshahi et al. [71]. The presence of micropores increases the surface area inside the porous structure for the nitrogen molecules to interact with, and this aids in spreading of the nitrogen molecules into the structure, which rapidly increases the adsorbed volume of nitrogen inside the porous carbon structure [69]. It was also observed that, in the relative pressure range of 0.2 to 1.0, the nitrogen adsorption was almost constant since the nitrogen gas's monolayer formation is complete. Now, the nitrogen just builds up layers inside the pores and fills the whole structure. Once the structure gets filled with nitrogen, the BET surface area was calculated using the BET isotherm. The calculated BET surface area of the three porous structures annealed at 8000 K (AT8000), 6000 K (AT6000), and 4000 K (AT4000) respectively were found to be 464 m²/g, 906.7 m²/g, and 1485 m²/g. These results were consistent with the experimentally derived surface area reported by Lee et al. [68] and Mistar et al. [69]. From the BET surface area values, it could be inferred that annealing at a lower temperature could significantly contribute to increasing the surface area of the carbon system.

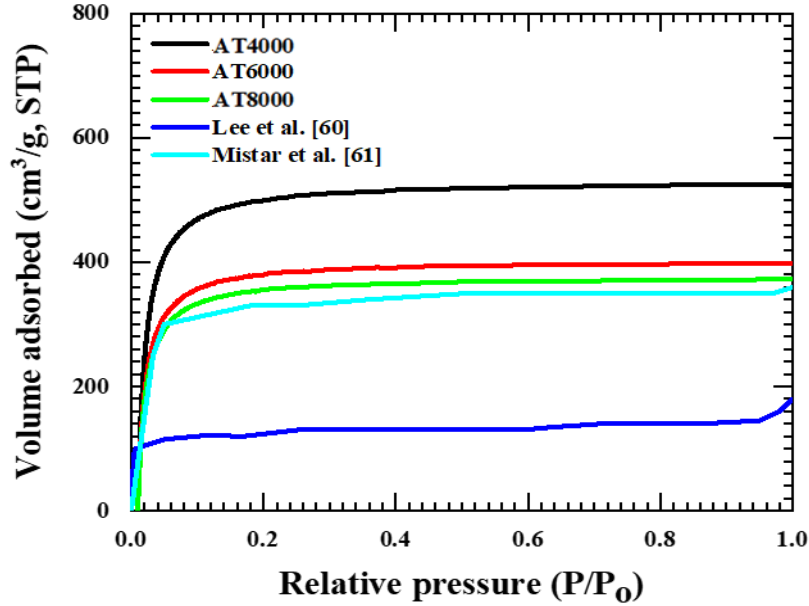


Fig. 8: BET adsorption isotherm for three porous carbon structures. The graph is in the form of a *Type I* BET adsorption isotherm, which represents the presence of a large volume of micropores. Micropores allow fast initial adsorption of N_2 molecules. Here, results are compared with the reported experimental results of Lee et al. [68] and Mistar et al. [69].

3.4 Intellectual merit of our model compared to the models suggested in literature

This study introduced a novel sphere pore modelling approach that differs from existing methods in several ways. We employ an iterative method to generate an exclusive sphere pore model. A summary of efforts comparing previously reported models in literature are anecdotally compared to our model in **Table 3**. A quantitative analysis was carried out to support this argument by comparing our model with Surface Geometry Reconstruction (SGR) model [33].

Proposed parameters such as the NNS and TAR facilitate throat quality assessment and improved network characterisation. Our focus on energy storage applications, particularly in understanding ion migration at the electrode-electrolyte interface, highlights the practical relevance of our method.

Table 3. Comparison between our model and previous models

Previous Models	Our model
<p>1. <u>Statistical reconstruction</u>: This method analyses the 2D cross-sectional images of the porous material to identify the geometrical features and reconstruct the 3D images of the same. Porosity and spatial distance between pores are the features that are used to reconstruct the 3D images [72]. Further properties like length of the pore chord, and distribution of linear paths were also used to characterize pore geometry [73–75]. However, these techniques do not successfully capture the initial geometry of the pore over longer distances.</p>	<p>One advantage of our model is the identification of long-range pore interconnectivity by using the concept of pores and throats that we adopted in this study (<i>refer Fig. 6</i>)</p>
<p>2. <u>Grain-based model</u>: The method randomly packs equal sized spheres to characterize the porous structure. Then the spatial arrangement of the spheres is varied in the vertical direction until the spheres overlap and describes porosity and pore connectivity of the structure. The developed method aided in understanding various physical and elastic properties of different porous structures [26]. Later, this method was further modified by Bakke et al. [76] to characterize porous structures using spheres of different sizes.</p>	<p>However, their model fails to capture microporosity of the porous media. Our current model has identified both these drawbacks and has been developed to incorporate different sized spheres as well as capture information of hierarchical pore size distribution. The algorithm works as per the flowchart in Fig. 2(b).</p>
<p>3. <u>Direct mapping model</u>: This model is subdivided into two types as discussed below</p>	
<p>3a) <u>Medial axis method</u>: The method constructs an medial axis passing through the pore space to represent the structural framework of the pore network by a thinning algorithm or a pore-space burning algorithm [77]. By employing the concept of medial axis, the model conserves the mathematical representation of the structural framework of the porous space, however identifying pores is still an issue.</p>	<p>Our model can measure both the pore size as well as the interconnected length of the porous structure using sphere pore model and NNS analysis</p>
<p>3b) <u>Maximal ball algorithm</u>: The method fits maximal spheres to occupy the porous space in the structure. Overlapping spheres are removed from the structure and remaining spheres (maximal balls) are fixed to describe the porous structure. The biggest maximal balls are used to determine the pores, which are connected by smaller balls in between them (these balls are called throats) [29]. The model</p>	<p>One of the problems with maximal ball algorithm is the specific identification of pores and throats in complex structures. Additionally, the algorithm identifies too many small throats that affects accuracy particularly if application is oriented in identifying microporosity. In our study, we have adopted two different steps to</p>

<p>utilizes high computer memory, time and was limited to be used in porous structures with relatively small and only has fewer pores less than thousand. Hence, Dong et al. [78] developed a search algorithm to identify the pore geometry. Bhattad et al. [31] used the same method to estimate the pore density of the medium.</p>	<p>mitigate these issues. The first step is to develop the sphere pore model with radii of best-fitted sphere pores (sphere pore model). The second step in mitigating the issue of too many throats were addressed by using the concept of nearest neighbor search (NNS) algorithm.</p>
<p>4. <u>Regular network model</u>: The model employs geometric shapes to capture the geometric features and characterize the pores and throats. Hence, the model is more efficient with respect to the time and also captures the minute features of the pores in the structure. Originally, a geometry with a cubic lattice and a constant coordination number of six was employed to characterise the porous media [79]. However, in porous media, the pore connectivity is distributed and can have a coordination number larger than six [78]. Therefore, models that employs the 26 pore coordination numbers concept were latter developed [80].</p>	<p>One of the drawbacks of such models is to identify porous networks for irregular or complex structures. Our model can identify both regular as well as complex structures and determine all parameters related to the structure such as size, shape, interconnectivity in quick time.</p>
<p>5. <u>Two-scale pore network model</u>: This model extracts features related to porosity (pore network) at different scales (micro, meso, etc.). The extracted features are latter merged by considering the cross-sectional similarities to create complete pore network. One disadvantage of this model is that it is computationally more expensive due to the number of network elements [81].</p>	<p>A major advantage of our model is its robustness wherein the algorithm can incorporate hierarchical porosity distribution without the need for adding complexity to the system.</p>
<p>6. <u>Surface geometry reconstruction (SGR) model</u>: SGR model is used to characterise porous structures by computing features such as surface area and porosity [33]. SGR model integrates the concept of Delaunay tessellation to fill the 3D porous structure with repeated tetrahedral regions of unit size that fit together closely without gaps or overlap. Afterwards, these regions are grouped and classified into spatially filled/empty regions by using virtual probe spheres of predefined fixed diameters. Tessellates are classified empty, if the probe sphere can be fitted into the region without overlapping with existing atoms in the porous structure. After classifying the tessellates into filled and empty regions, surface manifold will be</p>	<p>SGR model focuses on determining total pore count and total pore volume rather than the size of pores present in the structure. Our model gives quantitative insights into the nature of porosity (macro, meso, micro, etc.) as well as the pore interconnectivity</p>

developed to differentiate between these spaces. As these surface manifolds represent the boundaries of the porous atomic system, it aids in understanding about the filled and empty regions thus characterising porosity of the input porous structures.

Using SGR model, the features of the three porous carbon structures (AT4000, AT6000, AT8000) were quantitatively characterised. The respective porous carbon structures were tessellated into tetrahedral regions, and then these regions were classified as empty or filled to compute its features related to porosity. Furthermore, the results obtained from the SGR model was used to assess and compare with our model. SGR model was implemented using Ovito Pro [49]. The results computed by employing SGR model to characterise our three porous carbon structures (AT4000, AT6000, and AT8000) are shown in **Fig. 9** and *Table 4*.

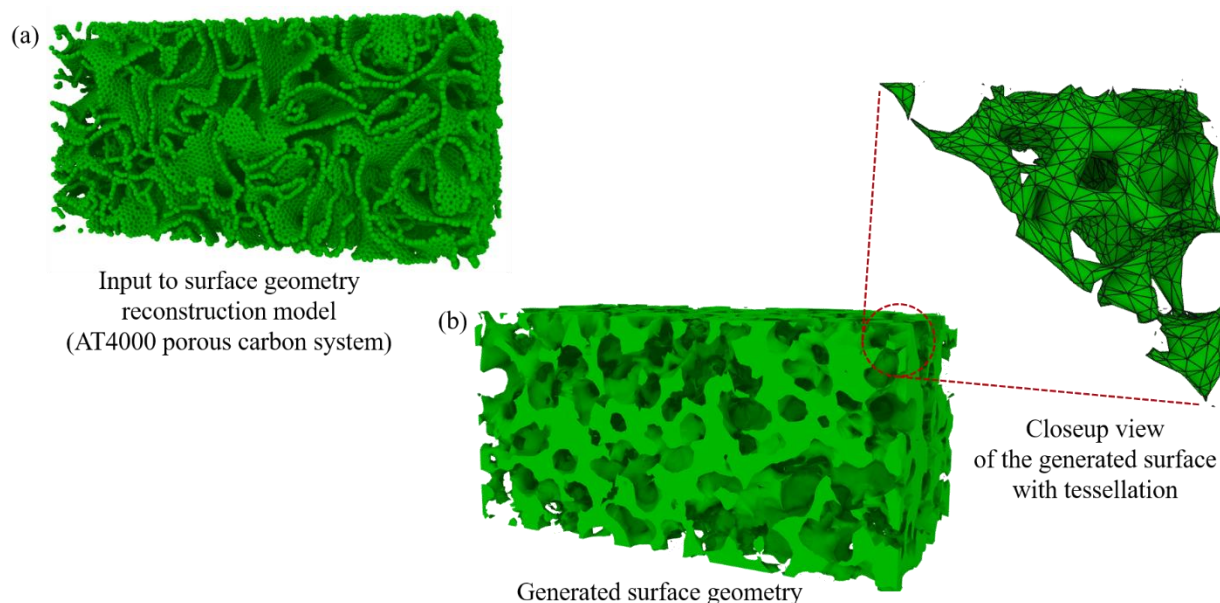


Fig. 9: (a) Isometric view of the AT4000 porous carbon system which was given into the surface geometry reconstruction model. (b) The geometric surface which was generated by the model along with the closeup view of a corner with tetragonal tessellation.

Table 4. Porous carbon structure analysis using SGR model and our model.

Porous structure	Empty fraction (%)			Total pore volume (\AA^3)			Total number of pores			NNS number coefficient (new detail from Our model)
	SGR		Our model	SGR		Our model	SGR		Our model	
	R_1^*	R_2^*		R_1^*	R_2^*		R_1^*	R_2^*		
Case – 1 (AT8000)	23.3	21.5	20.4	483378	447050	422443	93	233	5461	1.62
Case – 2 (AT6000)	24.3	23.3	22.9	504476	483470	474213	82	226	5307	1.66
Case – 3 (AT4000)	30.5	39.4	25.6	632011	819567	530125	21	54	5153	1.92

* $R_1 = 0.4$ nm and $R_2 = 0.5$ nm were the sphere radius used for calculating the SGR results

From **Table 4**, it could be observed that the results obtained from the SGR model vary with the radius of sphere (required manual input) used for the calculation. Our model works automatically by using the radii of best fitted spheres revealing optimal numbers. SGR model uses the concept of Delaunay tessellation to fill the three-dimensional porous carbon structure with repeated tetrahedral regions of unit size. These regions are fit together closely without gaps or overlap to compute characteristic features (pore count, pore volume and empty fraction) to define the porosity of the carbon structures (as shown in *Fig. 10 (a)*). On the other hand, our model uses the technique of filling the structure with radii of best-fitted sphere (sphere pore model) that are found using multiple iterations to completely occupy the pore volume structures (as shown in *Fig. 10 (b)*).

Compared to the SGR model, the optimal sized spheres fitted into the structure (sphere pore model) revealed more better measurable insights into the nature of porosity (macro, meso, micro, etc.). Additionally, our model also determined the total pore count and pore volume with better accuracy as compared to the SGR model as it takes into account all the representative spheres that constitute the pores while the accuracy of SGR depends on single pore size for calculations. Clearly, the proposed model outbids the SPR model and provide better estimates of the porosity.

Moreover, our model contrary to the SGR model provides insights into the pore connectivity and channels that are present in the structures, which is a significant factor in determining the performance of the electrodes for energy storage devices. Our model provided additional other details such as mean pore diameter, pore volume, pore size distribution and the NNS number as distinctive features which is in contrast to any of the previously reported models.

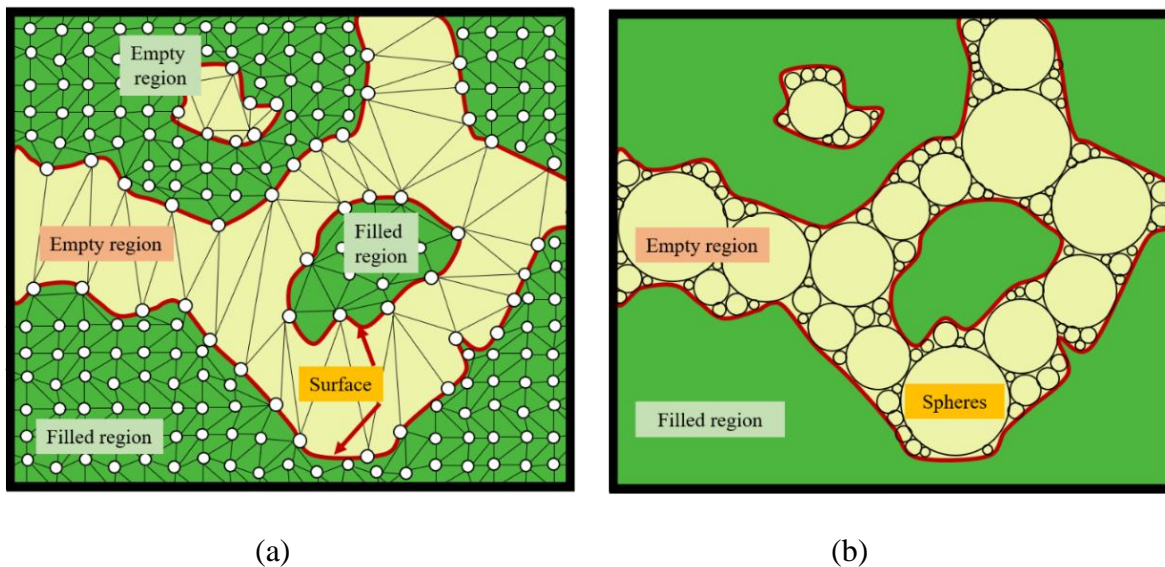


Fig. 10: (a) Tetragonal tessellation employed by the SGR model to estimate the empty region (porosity) in the given structure. (b) the newly proposed porosity estimation model after fitting spheres into the porous structure.

4. Conclusion

We propose the development of a novel sphere pore method for accurate quantitative assessment of porosity in a given material system. Building on a molecular dynamics simulation testbed performed on a porous carbon structure using the Gaussian Approximation Potential (GAP), we have thoroughly characterised the influence of annealing temperature and showed how porosity is influenced by the annealing parameters. Using our newly proposed strategy, we report a new nearest neighbour search (NNS) procedure, to quantify the interconnected throats. We characterised the pore sizes to estimate the ionic movement passing through the pores which would

aid in better design of electrodes for energy storage and conversion devices. The NNS coefficient was introduced to quantify the pore connectivity, networking, and degree of homogeneity of the pores and throats in porous carbon materials that could potentially be used to design porous electrodes. The NNS coefficient was highest for the annealing temperature of 4000 K as opposed to 8000K and that the formation of large pores in porous carbon material system in the size range of 1.4 nm to 1.7 nm is only likely for the annealing temperature of 4000 K but not for 6000 K or 8000 K. We compared these results through a simulated BET analysis and the Surface geometry reconstruction (SGR) model to observe robustness in our proposed model. This additional analysis revealed that more micropores formation is likely at higher annealing temperatures, whereas lower annealing temperature lead to an increased surface area through formation of larger graphitic ribbons.

Supplementary Materials

Supplementary information can be found here.

Author contributions

MN – Data curation, Formal Analysis, Investigation, Software, Writing – original draft

AK – Data curation, Formal Analysis, Investigation, Methodology, Software, Writing – original draft

AO – Data curation, Formal Analysis, Investigation, Methodology, Visualization, Writing – original draft

IRC – Data curation, Formal Analysis, Investigation, Software, Visualization

SB – Investigation, Supervision, Writing – review & editing

RRM – Investigation, Supervision, Writing – review & editing

SG – Data curation, Funding acquisition, Formal Analysis, Software, Supervision, Visualization,
Writing – review & editing

TR – Conceptualization, Funding acquisition, Project administration, Resources, Supervision,
Writing –review & editing

Conflicts of interest

There are no conflicts to declare.

Research data Statement

The raw data being reported in this paper can be obtained from the corresponding author upon reasonable request.

Acknowledgements

TR acknowledges the financial support provided by Science and Engineering Research Board (SERB), Government of India (SRG/2021/000741). SG acknowledge the financial support provided by the UKRI via Grant No. EP/T024607/1, the Hubert Curien Partnership award 2022 from the British Council and the International exchange Cost Share award by the Royal Society (IEC\NSFC\223536). Additionally, we are grateful to be granted the access of various HPC resources including BITS Pilani HPC cluster (Pilani campus & Sharanga), the Isambard Bristol, UK supercomputing service as well as Kittrick (LSBU, UK).

References

- [1] T. Roy, S. Goel, L.T. Costa, M.-M. Titirici, G.J. Offer, M. Marinescu, H. Wang, Strain induced electrochemical behaviors of ionic liquid electrolytes in an electrochemical double layer capacitor: Insights from molecular dynamics simulations, *J. Chem. Phys.* 159 (2023). <https://doi.org/10.1063/5.0166976>.
- [2] M. Fazeli Jadidi, H.Ö. Özer, S. Goel, J.I. Kilpatrick, N. McEvoy, D. McCloskey, J.F. Donegan, G.L.W. Cross, Distribution of shallow NV centers in diamond revealed by photoluminescence spectroscopy and nanomachining, *Carbon N. Y.* 167 (2020) 114–121. <https://doi.org/10.1016/j.carbon.2020.04.086>.
- [3] S.L. Candelaria, Y. Shao, W. Zhou, X. Li, J. Xiao, J.-G. Zhang, Y. Wang, J. Liu, J. Li, G. Cao, Nanostructured carbon for energy storage and conversion, *Nano Energy.* 1 (2012) 195–220. <https://doi.org/10.1016/j.nanoen.2011.11.006>.
- [4] B. Pal, S. Yang, S. Ramesh, V. Thangadurai, R. Jose, Electrolyte selection for supercapacitive devices: a critical review, *Nanoscale Adv.* 1 (2019) 3807–3835. <https://doi.org/10.1039/C9NA00374F>.
- [5] M. ben ben Mosbah, L. Mechi, R. Khiari, Y. Moussaoui, Current State of Porous Carbon for Wastewater Treatment, *Processes.* 8 (2020) 1651. <https://doi.org/10.3390/pr8121651>.
- [6] L. Chen, T. Ji, L. Mu, Y. Shi, H. Wang, J. Zhu, Pore size dependent molecular adsorption of cationic dye in biomass derived hierarchically porous carbon, *J. Environ. Manage.* 196 (2017) 168–177. <https://doi.org/10.1016/j.jenvman.2017.03.013>.
- [7] T. Liu, G. Liu, Porous organic materials offer vast future opportunities, *Nat. Commun.* 11 (2020) 4984. <https://doi.org/10.1038/s41467-020-15911-8>.
- [8] P. Zhu, P.R. Slater, E. Kendrick, Insights into architecture, design and manufacture of

- electrodes for lithium-ion batteries, *Mater. Des.* 223 (2022) 111208.
<https://doi.org/10.1016/j.matdes.2022.111208>.
- [9] Z. Pan, J. Yang, J. Kong, X.J. Loh, J. Wang, Z. Liu, “Porous and Yet Dense” Electrodes for High-Volumetric-Performance Electrochemical Capacitors: Principles, Advances, and Challenges, *Adv. Sci.* 9 (2022) 2103953. <https://doi.org/10.1002/advs.202103953>.
- [10] V.S. Bhat, S. S, T.J. Jayeoye, T. Rujiralai, U. Sirimahachai, K.F. Chong, G. Hegde, Influence of surface properties on electro-chemical supercapacitors utilizing *Callerya atropurpurea* pod derived porous nanocarbons: Structure property relationship between porous structures to energy storage devices, *Nano Sel.* 1 (2020) 226–243.
<https://doi.org/10.1002/nano.202000013>.
- [11] B.X. Medina-Rodriguez, V. Alvarado, Use of Gas Adsorption and Inversion Methods for Shale Pore Structure Characterization, *Energies.* 14 (2021) 2880.
<https://doi.org/10.3390/en14102880>.
- [12] H. Mashhadimoslem, M. Safarzadeh Khosrowshahi, M. Jafari, A. Ghaemi, A. Maleki, Adsorption Equilibrium, Thermodynamic, and Kinetic Study of O₂/N₂/CO₂ on Functionalized Granular Activated Carbon, *ACS Omega.* 7 (2022) 18409–18426.
<https://doi.org/10.1021/acsomega.2c00673>.
- [13] S.Z. Naqvi, J. Ramkumar, K.K. Kar, Functionalization of fly ash, in: *Handb. Fly Ash*, Elsevier, 2022: pp. 35–55. <https://doi.org/10.1016/B978-0-12-817686-3.00012-8>.
- [14] G. Fagerlund, Determination of specific surface by the BET method, *Matériaux Constr.* 6 (1973) 239–245. <https://doi.org/10.1007/BF02479039>.
- [15] P. Sinha, A. Datar, C. Jeong, X. Deng, Y.G. Chung, L.-C. Lin, Surface Area Determination of Porous Materials Using the Brunauer–Emmett–Teller (BET) Method:

- Limitations and Improvements, *J. Phys. Chem. C*. 123 (2019) 20195–20209.
<https://doi.org/10.1021/acs.jpcc.9b02116>.
- [16] P.I. Ravikovitch, G.L. Haller, A. V. Neimark, Density functional theory model for calculating pore size distributions: pore structure of nanoporous catalysts, *Adv. Colloid Interface Sci.* 76–77 (1998) 203–226. [https://doi.org/10.1016/S0001-8686\(98\)00047-5](https://doi.org/10.1016/S0001-8686(98)00047-5).
- [17] M.H. Joo, S.J. Park, S.-M. Hong, C.K. Rhee, D. Kim, G. Ji, S.W. Lee, Y. Sohn, X-ray micro computed tomography and efficient electrochemical recovery of lanthanides on porous carbon cylinder electrodes, *Compos. Part B Eng.* 231 (2022) 109590.
<https://doi.org/10.1016/j.compositesb.2021.109590>.
- [18] L. Magagnin, L. Nobili, P.L. Cavallotti, Metastable zinc–nickel alloys deposited from an alkaline electrolyte, *J. Alloys Compd.* 615 (2014) S444–S447.
<https://doi.org/10.1016/j.jallcom.2014.01.240>.
- [19] C.T.G. Smith, C.A. Mills, S. Pani, R. Rhodes, J.J. Bailey, S.J. Cooper, T.S. Pathan, V. Stolojan, D.J.L. Brett, P.R. Shearing, S.R.P. Silva, X-ray micro-computed tomography as a non-destructive tool for imaging the uptake of metal nanoparticles by graphene-based 3D carbon structures, *Nanoscale*. 11 (2019) 14734–14741.
<https://doi.org/10.1039/C9NR03056E>.
- [20] J. Le Houx, D. Kramer, Physics based modelling of porous lithium ion battery electrodes—A review, *Energy Reports*. 6 (2020) 1–9.
<https://doi.org/10.1016/j.egy.2020.02.021>.
- [21] K. Kirchner, T. Kirchner, V. Ivaništšev, M. V. Fedorov, Electrical double layer in ionic liquids: Structural transitions from multilayer to monolayer structure at the interface, *Electrochim. Acta*. 110 (2013) 762–771. <https://doi.org/10.1016/j.electacta.2013.05.049>.

- [22] Y. Zhou, H. Wang, Molecular Dynamics Simulation of a Single Carbon Chain through an Asymmetric Double-Layer Graphene Nanopore for Prolonging the Translocation Time, *ACS Omega*. 7 (2022) 16422–16429. <https://doi.org/10.1021/acsomega.2c00438>.
- [23] P. Vélez, G.L. Luque, D.E. Barraco, A.A. Franco, E.P.M. Leiva, Pore size distribution of carbon black: An approach from a coarse-grained potential, *Comput. Mater. Sci.* 209 (2022) 111409. <https://doi.org/10.1016/j.commatsci.2022.111409>.
- [24] J. Wang, C.L. Liu, Molecular Dynamics Simulation for Temperature and Graphite-Like Structure Effects on Amorphous Carbon Graphitization, *Mater. Sci. Forum.* 956 (2019) 78–86. <https://doi.org/10.4028/www.scientific.net/MSF.956.78>.
- [25] Z. Bo, C. Li, H. Yang, K. Ostrikov, J. Yan, K. Cen, Design of Supercapacitor Electrodes Using Molecular Dynamics Simulations, *Nano-Micro Lett.* 10 (2018) 1–23. <https://doi.org/10.1007/s40820-018-0188-2>.
- [26] S. Bryant, M. Blunt, Prediction of relative permeability in simple porous media, *Phys. Rev. A*. 46 (1992) 2004–2011. <https://doi.org/10.1103/PhysRevA.46.2004>.
- [27] S.L. Bryant, D.W. Mellor, C.A. Cade, Physically representative network models of transport in porous media, *AIChE J.* 39 (1993) 387–396. <https://doi.org/10.1002/aic.690390303>.
- [28] S.L. Bryant, P.R. King, D.W. Mellor, Network model evaluation of permeability and spatial correlation in a real random sphere packing, *Transp. Porous Media.* 11 (1993) 53–70. <https://doi.org/10.1007/BF00614635>.
- [29] D. Silin, T. Patzek, Pore space morphology analysis using maximal inscribed spheres, *Phys. A Stat. Mech. Its Appl.* 371 (2006) 336–360. <https://doi.org/10.1016/j.physa.2006.04.048>.

- [30] A.S. Al-Kharusi, M.J. Blunt, Network extraction from sandstone and carbonate pore space images, *J. Pet. Sci. Eng.* 56 (2007) 219–231. <https://doi.org/10.1016/j.petrol.2006.09.003>.
- [31] P. Bhattad, C.S. Willson, K.E. Thompson, Effect of Network Structure on Characterization and Flow Modeling Using X-ray Micro-Tomography Images of Granular and Fibrous Porous Media, *Transp. Porous Media.* 90 (2011) 363–391. <https://doi.org/10.1007/s11242-011-9789-7>.
- [32] A. Gayon Lombardo, B.A. Simon, O. Taiwo, S.J. Neethling, N.P. Brandon, A pore network model of porous electrodes in electrochemical devices, *J. Energy Storage.* 24 (2019) 100736. <https://doi.org/10.1016/j.est.2019.04.010>.
- [33] A. Stukowski, Computational analysis methods in atomistic modeling of crystals, *Jom.* 66 (2014) 399–407. <https://doi.org/10.1007/s11837-013-0827-5>.
- [34] A. Khaitan, A. Owhal, S.U. Belgamwar, R. Raman Mishra, S. Goel, T. Roy, Designing porous electrode structures for supercapacitors using quenched MD simulations, *Mater. Today Proc.* (2022). <https://doi.org/10.1016/j.matpr.2022.03.726>.
- [35] S.J. Stuart, A.B. Tutein, J.A. Harrison, A reactive potential for hydrocarbons with intermolecular interactions, *J. Chem. Phys.* 112 (2000) 6472–6486. <https://doi.org/10.1063/1.481208>.
- [36] C. Qian, B. McLean, D. Hedman, F. Ding, A comprehensive assessment of empirical potentials for carbon materials, *APL Mater.* 9 (2021) 061102. <https://doi.org/10.1063/5.0052870>.
- [37] Y. Wang, Z. Fan, P. Qian, T. Ala-Nissila, M.A. Caro, Structure and Pore Size Distribution in Nanoporous Carbon, *Chem. Mater.* 34 (2022) 617–628. <https://doi.org/10.1021/ACS.CHEMMATER.1C03279/ASSET/IMAGES/LARGE/CM1C>

03279_0011.JPEG.

- [38] V.L. Deringer, G. Csányi, Machine learning based interatomic potential for amorphous carbon, *Phys. Rev. B.* 95 (2017) 094203. <https://doi.org/10.1103/PhysRevB.95.094203>.
- [39] C. de Tomas, I. Suarez-Martinez, F. Vallejos-Burgos, M.J. López, K. Kaneko, N.A. Marks, Structural prediction of graphitization and porosity in carbide-derived carbons, *Carbon N. Y.* 119 (2017) 1–9. <https://doi.org/10.1016/j.carbon.2017.04.004>.
- [40] C. de Tomas, A. Aghajamali, J.L. Jones, D.J. Lim, M.J. López, I. Suarez-Martinez, N.A. Marks, Transferability in interatomic potentials for carbon, *Carbon N. Y.* 155 (2019) 624–634. <https://doi.org/10.1016/j.carbon.2019.07.074>.
- [41] A.C. Ferrari, A. Libassi, B.K. Tanner, V. Stolojan, J. Yuan, L.M. Brown, S.E. Rodil, B. Kleinsorge, J. Robertson, Density, sp³ fraction, and cross-sectional structure of amorphous carbon films determined by x-ray reflectivity and electron energy-loss spectroscopy, *Phys. Rev. B.* 62 (2000) 11089–11103. <https://doi.org/10.1103/PhysRevB.62.11089>.
- [42] D.G. McCulloch, D.R. McKenzie, C.M. Goringe, Ab initio simulations of the structure of amorphous carbon, *Phys. Rev. B.* 61 (2000) 2349–2355. <https://doi.org/10.1103/PhysRevB.61.2349>.
- [43] A.M. Ito, A. Takayama, Y. Oda, H. Nakamura, The First principle calculation of bulk modulus and Young's modulus for amorphous carbon material, *J. Phys. Conf. Ser.* 518 (2014) 012011. <https://doi.org/10.1088/1742-6596/518/1/012011>.
- [44] J. Schwan, S. Ulrich, H. Roth, H. Ehrhardt, S.R.P. Silva, J. Robertson, R. Samlenski, R. Brenn, Tetrahedral amorphous carbon films prepared by magnetron sputtering and dc ion plating, *J. Appl. Phys.* 79 (1996) 1416–1422. <https://doi.org/10.1063/1.360979>.

- [45] S. Gavaldà, K.E. Gubbins, Y. Hanzawa, K. Kaneko, K.T. Thomson, Nitrogen adsorption in carbon aerogels: A molecular simulation study, *Langmuir*. 18 (2002) 2141–2151. <https://doi.org/10.1021/LA011132O/ASSET/IMAGES/MEDIUM/LA011132OE00011.GIF>.
- [46] P. Ranjan, A. Owhal, D. Chakrabarti, S.U. Belgamwar, T. Roy, R. Balasubramaniam, Fundamental insights of mechanical polishing on polycrystalline Cu through molecular dynamics simulations, *Mater. Today Commun.* 32 (2022) 103980. <https://doi.org/10.1016/j.mtcomm.2022.103980>.
- [47] K. Vollmayr-Lee, Introduction to molecular dynamics simulations, *Am. J. Phys.* 88 (2020) 401–422. <https://doi.org/10.1119/10.0000654>.
- [48] A.Z. AL Shaqsi, K. Sopian, A. Al-Hinai, Review of energy storage services, applications, limitations, and benefits, *Energy Reports*. 6 (2020) 288–306. <https://doi.org/10.1016/j.egyr.2020.07.028>.
- [49] A. Stukowski, V. V. Bulatov, A. Arsenlis, Automated identification and indexing of dislocations in crystal interfaces, *Model. Simul. Mater. Sci. Eng.* 20 (2012) 085007. <https://doi.org/10.1088/0965-0393/20/8/085007>.
- [50] H. Tachikawa, T. Iyama, Mechanism of Hydrogen Storage in the Graphene Nanoflake–Lithium–H₂ System, *J. Phys. Chem. C*. 123 (2019) 8709–8716. <https://doi.org/10.1021/acs.jpcc.9b01152>.
- [51] R. Bardestani, G.S. Patience, S. Kaliaguine, Experimental methods in chemical engineering: specific surface area and pore size distribution measurements—BET, BJH, and DFT, *Can. J. Chem. Eng.* 97 (2019) 2781–2791. <https://doi.org/10.1002/cjce.23632>.
- [52] A. Torres-Knoop, A. Poursaeidesfahani, T.J.H. Vlugt, D. Dubbeldam, Behavior of the

- Enthalpy of Adsorption in Nanoporous Materials Close to Saturation Conditions, *J. Chem. Theory Comput.* 13 (2017) 3326–3339. <https://doi.org/10.1021/acs.jctc.6b01193>.
- [53] J.-T. Wang, C. Chen, E. Wang, Y. Kawazoe, A New Carbon Allotrope with Six-Fold Helical Chains in all-sp² Bonding Networks, *Sci. Rep.* 4 (2014) 4339. <https://doi.org/10.1038/srep04339>.
- [54] Q. Xiong, T.G. Baychev, A.P. Jivkov, Review of pore network modelling of porous media: Experimental characterisations, network constructions and applications to reactive transport, *J. Contam. Hydrol.* 192 (2016) 101–117. <https://doi.org/10.1016/j.jconhyd.2016.07.002>.
- [55] L. Gong, L. Nie, Y. Xu, Geometrical and Topological Analysis of Pore Space in Sandstones Based on X-ray Computed Tomography, *Energies.* 13 (2020) 3774. <https://doi.org/10.3390/en13153774>.
- [56] S. Wang, D. Minami, K. Kaneko, Comparative pore structure analysis of highly porous graphene monoliths treated at different temperatures with adsorption of N₂ at 77.4 K and of Ar at 87.3 K and 77.4 K, *Microporous Mesoporous Mater.* 209 (2015) 72–78. <https://doi.org/10.1016/j.micromeso.2015.01.014>.
- [57] K. Koderu, Y. Onishi, The Molecular Cross-sectional Areas for the Determination of Specific Surface Areas of Solids. I. Carbon Black, *Bull. Chem. Soc. Jpn.* 32 (1959) 356–361. <https://doi.org/10.1246/bcsj.32.356>.
- [58] J. Zou, C. Fan, Y. Jiang, X. Liu, W. Zhou, H. Xu, L. Huang, A preliminary study on assessing the Brunauer-Emmett-Teller analysis for disordered carbonaceous materials, *Microporous Mesoporous Mater.* 327 (2021) 111411. <https://doi.org/10.1016/j.micromeso.2021.111411>.

- [59] C. de Tomas, I. Suarez-Martinez, F. Vallejos-Burgos, M.J. López, K. Kaneko, N.A. Marks, Structural prediction of graphitization and porosity in carbide-derived carbons, *Carbon N. Y.* 119 (2017) 1–9. <https://doi.org/10.1016/j.carbon.2017.04.004>.
- [60] C. de Tomas, I. Suarez-Martinez, N.A. Marks, Carbide-derived carbons for dense and tunable 3D graphene networks, *Appl. Phys. Lett.* 112 (2018) 251907. <https://doi.org/10.1063/1.5030136>.
- [61] M. Thompson, B. Dyatkin, H.-W. Wang, C. Turner, X. Sang, R. Unocic, C. Iacovella, Y. Gogotsi, A. van Duin, P. Cummings, An Atomistic Carbide-Derived Carbon Model Generated Using ReaxFF-Based Quenched Molecular Dynamics, *C—Journal Carbon Res.* 3 (2017) 32. <https://doi.org/10.3390/c3040032>.
- [62] T.B. Shiell, D.G. McCulloch, J.E. Bradby, B. Haberl, D.R. McKenzie, Neutron diffraction discriminates between models for the nanoarchitecture of graphene sheets in glassy carbon, *J. Non. Cryst. Solids.* 554 (2021) 120610. <https://doi.org/10.1016/j.jnoncrysol.2020.120610>.
- [63] J.C. Palmer, A. Llobet, S.-H. Yeon, J.E. Fischer, Y. Shi, Y. Gogotsi, K.E. Gubbins, Modeling the structural evolution of carbide-derived carbons using quenched molecular dynamics, *Carbon N. Y.* 48 (2010) 1116–1123. <https://doi.org/10.1016/j.carbon.2009.11.033>.
- [64] C. Largeot, C. Portet, J. Chmiola, P.L. Taberna, Y. Gogotsi, P. Simon, Relation between the ion size and pore size for an electric double-layer capacitor, *J. Am. Chem. Soc.* 130 (2008) 2730–2731. <https://doi.org/10.1021/ja7106178>.
- [65] F.L.E. Usseglio-Viretta, D.P. Finegan, A. Colclasure, T.M.M. Heenan, D. Abraham, P. Shearing, K. Smith, Quantitative Relationships Between Pore Tortuosity, Pore Topology,

- and Solid Particle Morphology Using a Novel Discrete Particle Size Algorithm, *J. Electrochem. Soc.* 167 (2020) 100513. <https://doi.org/10.1149/1945-7111/ab913b>.
- [66] L.R. Jordan, A.K. Shukla, T. Behrsing, N.R. Avery, B.C. Muddle, M. Forsyth, Diffusion layer parameters influencing optimal fuel cell performance, *J. Power Sources.* 86 (2000) 250–254. [https://doi.org/10.1016/S0378-7753\(99\)00489-9](https://doi.org/10.1016/S0378-7753(99)00489-9).
- [67] L. Gong, L. Nie, Y. Xu, Geometrical and Topological Analysis of Pore Space in Sandstones Based on X-ray Computed Tomography, *Energies* 2020, Vol. 13, Page 3774. 13 (2020) 3774. <https://doi.org/10.3390/EN13153774>.
- [68] H.-M. Lee, H.-R. Kang, K.-H. An, H.-G. Kim, B.-J. Kim, Comparative studies of porous carbon nanofibers by various activation methods, *Carbon Lett.* 14 (2013) 180–185. <https://doi.org/10.5714/CL.2013.14.3.180>.
- [69] E.M. Mistar, T. Alfatah, M.D. Supardan, Synthesis and characterization of activated carbon from *Bambusa vulgaris striata* using two-step KOH activation, *J. Mater. Res. Technol.* 9 (2020) 6278–6286. <https://doi.org/10.1016/j.jmrt.2020.03.041>.
- [70] F. Ambroz, T.J. Macdonald, V. Martis, I.P. Parkin, Evaluation of the BET Theory for the Characterization of Meso and Microporous MOFs, *Small Methods.* 2 (2018) 1800173. <https://doi.org/10.1002/smtd.201800173>.
- [71] M.S. Khosrowshahi, M.A. Abdol, H. Mashhadimoslem, E. Khakpour, H.B.M. Emrooz, S. Sadeghzadeh, A. Ghaemi, The role of surface chemistry on CO₂ adsorption in biomass-derived porous carbons by experimental results and molecular dynamics simulations, *Sci. Rep.* 12 (2022) 8917. <https://doi.org/10.1038/s41598-022-12596-5>.
- [72] P.M. Adler, J.F. Thovert, Real Porous Media: Local Geometry and Macroscopic Properties, *Appl. Mech. Rev.* 51 (1998) 537–585. <https://doi.org/10.1115/1.3099022>.

- [73] C.L.Y. Yeong, S. Torquato, Reconstructing random media, *Phys. Rev. E.* 57 (1998) 495. <https://doi.org/10.1103/PhysRevE.57.495>.
- [74] R. Hilfer, Geometric and dielectric characterization of porous media, *Phys. Rev. B.* 44 (1991) 60. <https://doi.org/10.1103/PhysRevB.44.60>.
- [75] P. Levitz, Off-lattice reconstruction of porous media: critical evaluation, geometrical confinement and molecular transport, *Adv. Colloid Interface Sci.* 76–77 (1998) 71–106. [https://doi.org/10.1016/S0001-8686\(98\)00042-6](https://doi.org/10.1016/S0001-8686(98)00042-6).
- [76] S. Bakke, P.E. Øren, 3-D Pore-Scale Modelling of Sandstones and Flow Simulations in the Pore Networks, *SPE J.* 2 (1997) 136–149. <https://doi.org/10.2118/35479-PA>.
- [77] Z.R. Liang, C.P. Fernandes, F.S. Magnani, P.C. Philippi, A reconstruction technique for three-dimensional porous media using image analysis and Fourier transforms, *J. Pet. Sci. Eng.* 21 (1998) 273–283. [https://doi.org/10.1016/S0920-4105\(98\)00077-1](https://doi.org/10.1016/S0920-4105(98)00077-1).
- [78] H. Dong, M.J. Blunt, Pore-network extraction from micro-computerized-tomography images, *Phys. Rev. E - Stat. Nonlinear, Soft Matter Phys.* 80 (2009) 036307. <https://doi.org/10.1103/PHYSREVE.80.036307/FIGURES/18/MEDIUM>.
- [79] M.A. Ioannidis, I. Chatzis, Network modelling of pore structure and transport properties of porous media, *Chem. Eng. Sci.* 48 (1993) 951–972. [https://doi.org/10.1016/0009-2509\(93\)80333-L](https://doi.org/10.1016/0009-2509(93)80333-L).
- [80] A. Raouf, S. Majid Hassanizadeh, A new method for generating pore-network models of porous media, *Transp. Porous Media.* 81 (2010) 391–407. <https://doi.org/10.1007/S11242-009-9412-3/METRICS>.
- [81] T. Bultreys, L. Van Hoorebeke, V. Cnudde, Multi-scale, micro-computed tomography-based pore network models to simulate drainage in heterogeneous rocks, *Adv. Water*

Resour. 78 (2015) 36–49. <https://doi.org/10.1016/J.ADVWATRES.2015.02.003>.